The Conveyor Belt of the Skies: Thermal Wind and the Jet Stream

Ian Jacobi

April 5, 2012

Abstract

The jet stream is a significant feature of the upper atmosphere generated by temperature gradients by a relation known as thermal wind. This paper examines the jet stream and thermal wind in detail, deriving the thermal wind from the geostrophic and ideal gas relations and explaining its relationship to the jet stream. A laboratory experiment is also presented to demonstrate the qualitative effects of the thermal wind in physical terms.

1 Introduction

Wind is one of the most important aspects of the atmosphere. Like other meteorological phenomena, wind has direct impacts on human life through its ability to wreak havoc directly in the form of both strong straight-line winds and tornadoes. In addition to this, wind also plays a more subtle role in which it is no less important; it is the movement of air and the accompanying related properties of a given air parcel, such as moisture, temperature and vertical instability.

Although we can understand wind in terms of the circular movement of air around high and low pressure systems through the twin concepts of geostrophic and cyclostrophic flow, such an understanding fails to explain how these high and low pressure systems form and move in the first place. Unless we have a mechanism to understand this movement, our understanding of the wind is of limited use.

We might be able to use wind to predict the location of high and low pressure systems, or vice versa, but unless we understand how those systems move, and where they are moving to, we cannot hope to even predict what the wind will be tomorrow, let alone the weather. There is, however, *one* wind which, if understood, might help us in our quest to make such predictive statements: the jet stream.

2   Phenomena: The Jet Stream

Perhaps the most striking feature of the atmosphere is the giant river of wind in the middle latitudes. This wind, called the *jet stream*, is significant not only for its size, but also for its role in forming and steering high and low pressure systems in the mid-latitudes, effectively driving much of the weather that affects North America, Europe, and East Asia through the inertial instability which accompanies a strong jet. [3]

The extent of the jet stream is readily visible in the tight banding of isoheight lines on any hemispherical pressure map taken above the 500mb level. Since, according to the geostrophic relationship,

$$\mathbf{u}_g = \frac{g}{f}\hat{\mathbf{z}} \times \nabla z, \tag{1}$$

it is possible to conclude that the tightly banded isoheights visible over the oceans in Figure 1 correspond to regions of extremely high winds. A plot of the wind vectors as wind barbs shows this assumption to be true (Figure 2).

The jet stream is not only striking for its narrow banding across only a few degrees of latitude, but also for its *vertical locality*. The strong winds of the jet stream are never observed at the surface of the Earth, but are entirely localized to the higher levels of the atmosphere, as can be seen in a vertical cross-section of the atmosphere taken along a line of longitude in Figure 3.

The presence of the jet stream raises many questions that, if answered, might give a better understanding of middle-latitude weather systems. Why is the jet stream so strong? Why is it tightly constrained to a band of only a few degrees latitude? Why is it present only at higher altitudes? To understand these questions, we must turn to the concept known as "thermal wind."

3   The Theory: Thermal Wind

The movement of wind in the jet stream can largely be explained by a phenomenon called thermal wind, which relates wind shear (the vertical difference in wind speed) to horizontal temperature gradients. [3] To understand thermal wind, however, one must first understand how the atmosphere behaves under different temperatures on a global scale.

Air tends to expand when heated. According to the ideal gas law in its molar form,

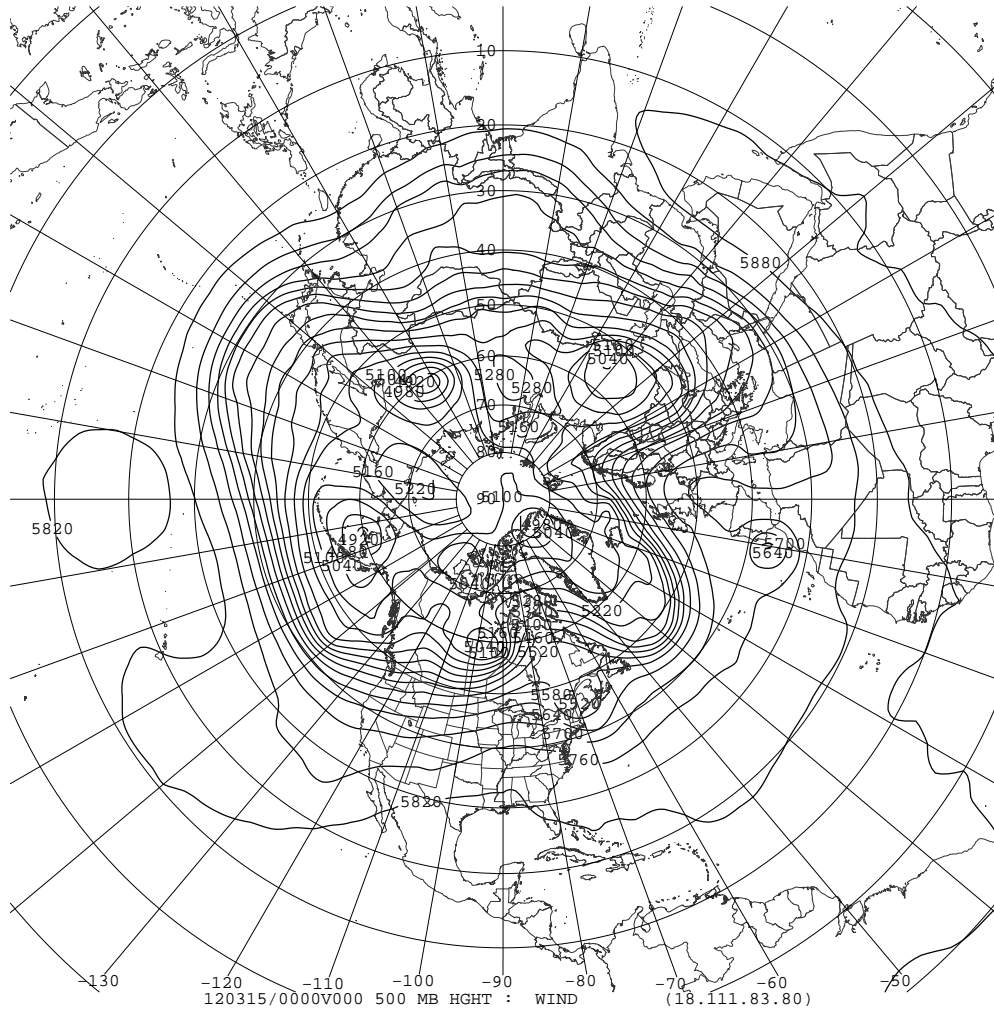$$P = \rho R_{\text{specific}}T, \tag{2}$$

Figure 1: Heights of the 500mb pressure surface in the Northern Hemisphere at 00:00 UTC on 15 March 2012. The height changes drastically across a narrow band that runs approximately along 45°N, implying a strong wind which winds around the world.
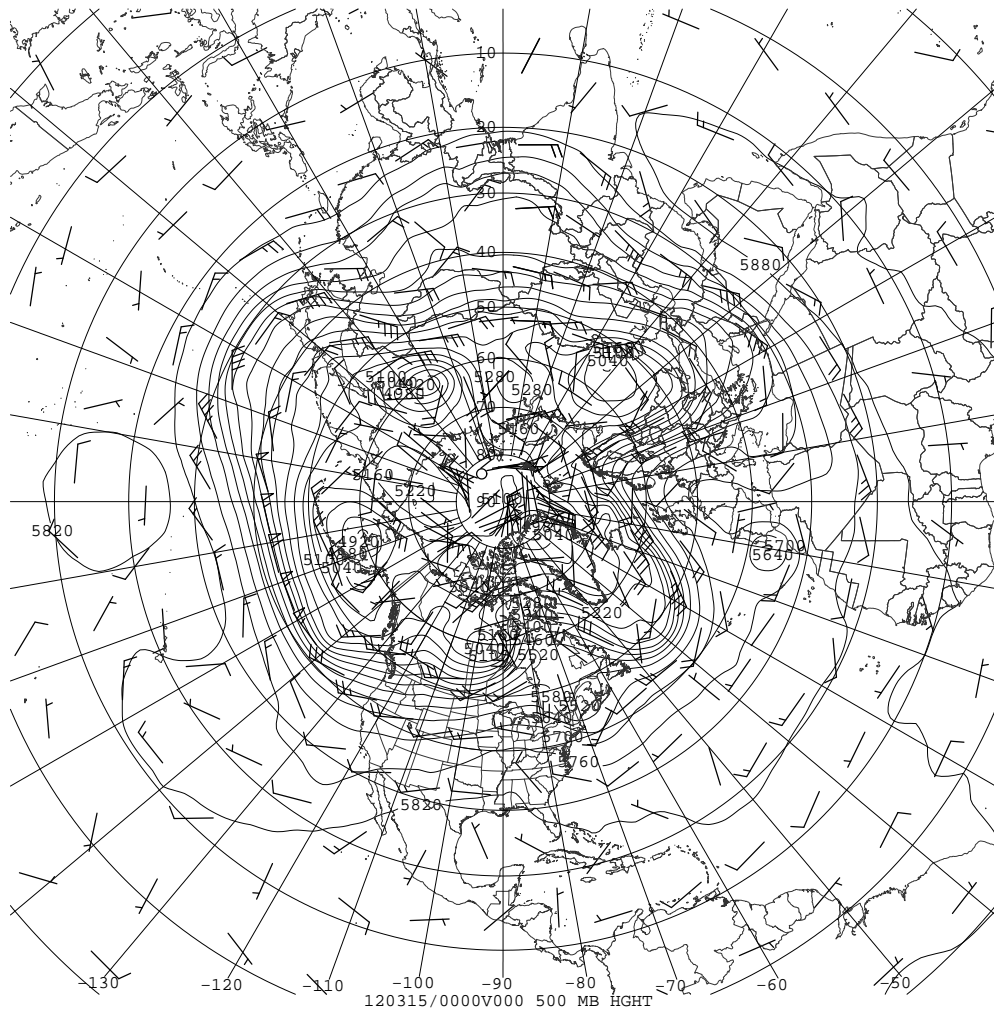
Figure 2: Heights and observed winds on the 500mb pressure surface in the Northern Hemisphere at 00:00 UTC on 15 March 2012. Winds are generally weak except along for a strong west-to-east wind along a narrow band at approximately 45°N latitude, where the height gradient is strong.
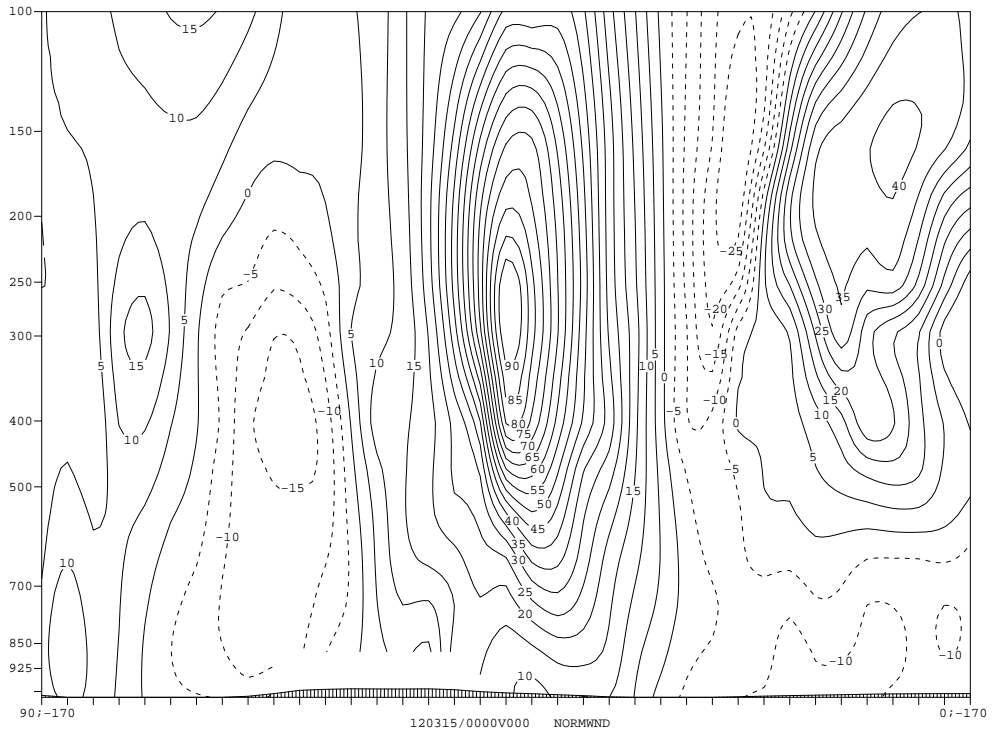
Figure 3: Windspeed normal to a north-south cross-section from the north pole to the equator along 170°W at 00:00 UTC on 15 March 2012. Positive values blow from west to east. The jet stream is localized high above the surface, ranging up to 90m/s at the 250mb level.
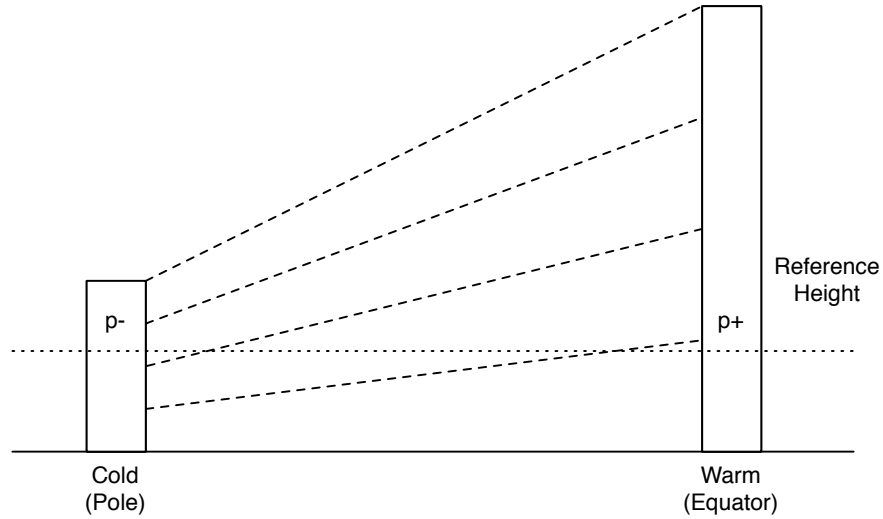
Figure 4: The temperature gradient between the poles and the equator causes differences in pressure heights due to the expansion of warmer air. The slope of a pressure surface thus increases with height.

given a constant pressure P, the density of a gas, ρ, must decrease as the temperature T increases (as defined by the specific gas constant, R). Thus, since the mass of a column of air at the poles and equator are approximately equal (as the pressure at the bottom of such a column is almost the same), the warmer temperature of tropical air implies that the density of that column must decrease, causing a corresponding increase in the height of that column of air. The difference in the height of this column between the poles and the equator creates a gradually increasing slope of pressure levels higher in the atmosphere (Figure 4).

This increasing slope of pressure levels necessarily translates to an increasing geostrophic wind speed with height when the Rossby number is much less than one. Indeed, from the zonal geostrophic wind relation at constant pressure,

$$\mathbf{u}_g = \frac{g}{f}\hat{\mathbf{z}} \times \nabla z,$$ (3)

it is possible to derive the relationship between horizontal temperature gradients and wind known as the *thermal wind equation*. [4]

3.1 Deriving the Geostrophic Wind Shear from Temperature

In order to relate the temperature gradient to wind shear, it must be the case that T may be introduced into Equation 3. The ideal gas equation, Equation 2 offers one way to do so thanks to its use of ρ, the density of the gas. As the pressure at a given height may be determined by the hydrostatic equation,

$$\frac{\partial p}{\partial z} = -\rho g, \tag{4}$$

in which ρ is the density of air, it is possible to take the reciprocal of this relation, $\frac{\partial z}{\partial p}$ and use it to introduce ρ into the geostrophic wind relation. This may be done by substituting the value for $\frac{\partial z}{\partial p}$ after taking the derivative of Equation 3 with respect to p. This gives the following:

$$\frac{\partial \mathbf{u}_g}{\partial p} = \frac{g}{f} \frac{\partial}{\partial z} \hat{\mathbf{z}} \times \nabla z$$

$$= -\frac{1}{f} \hat{\mathbf{z}} \times \nabla \frac{1}{\rho}, \tag{5}$$

where the derivative is again, taken in pressure coordinates.

With the relationship of the molar ideal gas law, given in Equation 2, it is possible to obtain this relationship in terms of temperature by substituting $\frac{1}{\rho} = \frac{RT}{p}$ into Equation 5, giving:

$$\frac{\partial \mathbf{u}_g}{\partial p} = -\frac{1}{f} \hat{\mathbf{z}} \times \nabla \frac{RT}{p}. \tag{6}$$

Factoring out R and p (the latter as the derivative is taken at constant p) gives the *thermal wind* relationship between a temperature gradient and the vertical *wind shear*:

$$\frac{\partial \mathbf{u}_g}{\partial p} = -\frac{R}{fp} \hat{\mathbf{z}} \times \nabla T. \tag{7}$$

3.2 The Polar Front and the Jet Stream

This thermal wind equation indicates that sharp horizontal temperature gradients will create vertical wind shear. The practical result of this relationship arises from the sharp temperature gradient that marks the boundary of cold polar air and warm tropical air in the middle latitudes (Figure 5).
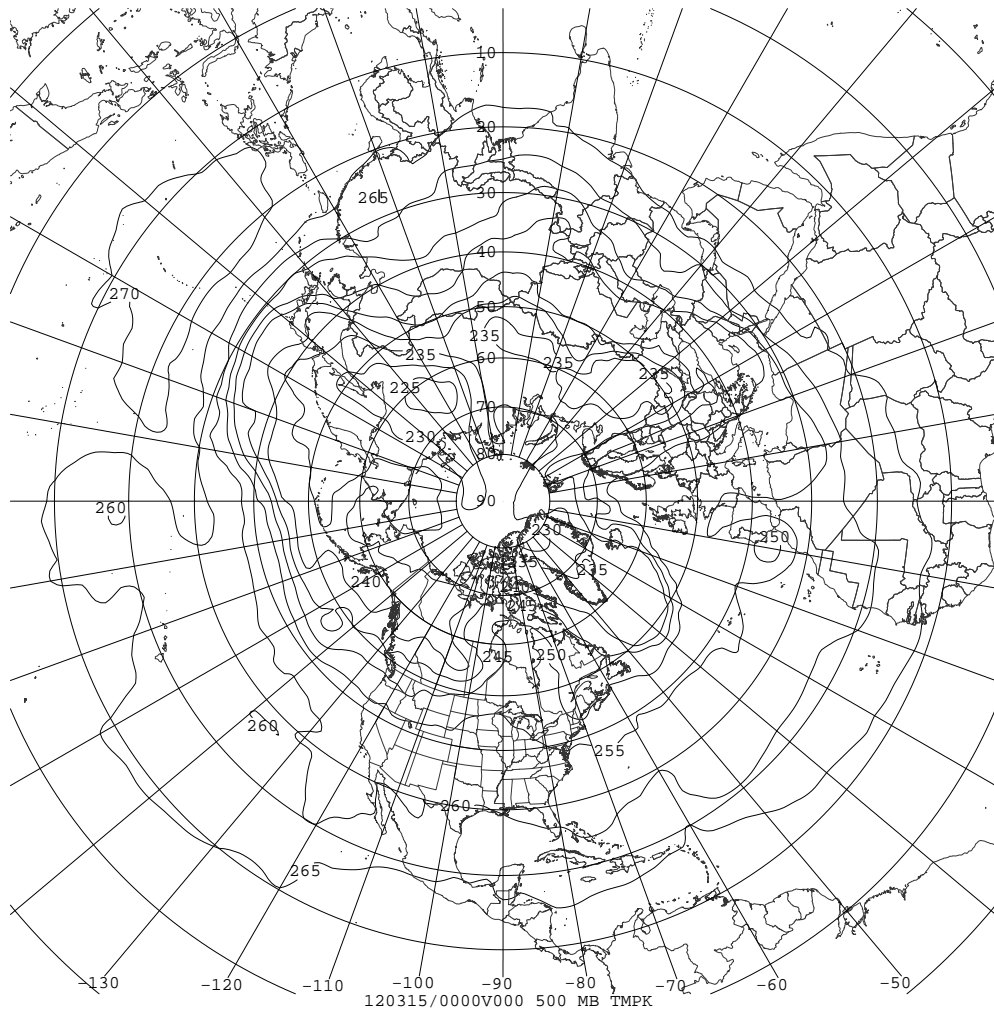
Figure 5: Temperatures at the 500mb pressure surface in the Northern Hemisphere at 00:00 UTC on 15 March 2012. A sharp temperature gradient is visible between about 38°N and 48°N.

The existence of this temperature gradient seems surprising at first glance. Why should such a sharp gradient exist? The answer lies in the relatively slow speed of mixing in air. What little mixing of air occurs largely takes place in the form of diffusion and conduction. This process is so slow as to be negligible. As such, rather than observing mixing, there is usually a distinct boundary between warm and cold air systems, called a *frontal boundary.*

The front between warm tropical air and cold polar air is called the *polar front.* The relative strength of this frontal boundary necessarily leads to strong wind shear and the jet stream. [4] Equipped with the Thermal Wind Equation, Equation 7, it is possible to calculate an approximation of the speed of the jet stream and verify its relationship to the polar front and the thermal wind.

Before we can do so, however, one problem must be addressed. The atmosphere is a compressible fluid. As such temperature varies with pressure and is not conserved. This may be observed in Figure 6, where the temperature decreases with height, as would be expected given the ideal gas law, Equation 2. This complication makes it difficult to discuss the temperature of the atmosphere without also discussing the pressure level at which it was measured.

To eliminate this issue, it is possible to construct a conserved measurement based on the temperature that does not vary with pressure by instead measuring the temperature an air parcel would have if taken adiabatically to a standard reference pressure p_0 of 1000 millibars. [3] This value, the *potential temperature*, is useful in many contexts including that of the thermal wind because the nature of atmosphere as a compressible fluid means that atmospheric science typically works in pressure coordinates. As such, a conserved temperature equivalent is necessary.

3.3   The Potential Temperature

Construction of the potential temperature θ may be done by considering the change in heat in an adiabatic process (one in which there is no change in entropy), where $dU = 0$. For such a process, the change in heat is defined, as always, by the first law of thermodynamics,

$$\delta Q = dU + pdV = c_v dT + pdV. \tag{8}$$

where Q is the amount of energy added to the system and dU is the change in internal energy in the system, related to the change in temperature and the specific heat capacity at constant volume via the relation $dU = c_v dT$.
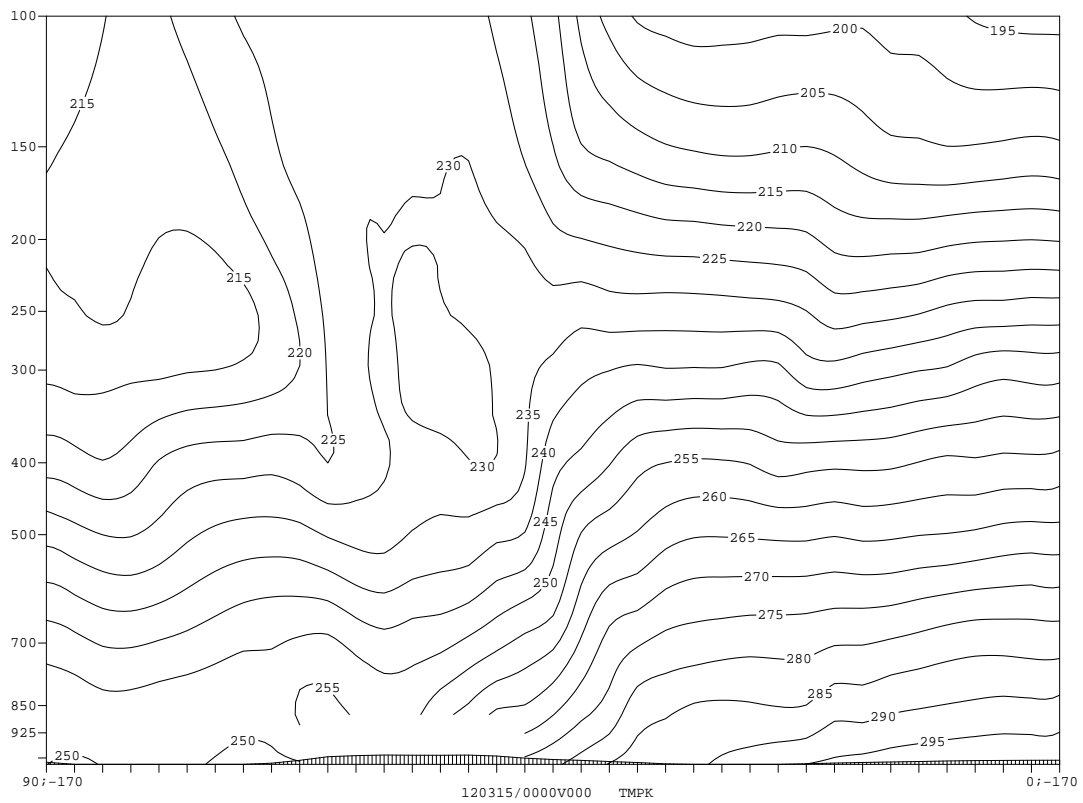
Figure 6: Cross-section of air temperature above 170°W longitude from the north pole to the equator as of 00:00 UTC on 15 March 2012. The temperature gradient near the 45th parallel is visible, as is the tendancy of temperature to decrease with height.

Taking the derivative of ideal gas law $pV = RT$ gives $V\,dp + p\,dV = R\,dT$, which may be rearranged to allow Equation 8 to be restated solely in terms of changes in pressure and temperature, as follows:

$$\delta Q = c_v dT + R dT - V\,dp. \tag{9}$$

The specific heat capacity at constant pressure, c_p, may be defined for an ideal gas in terms of the specific heat capacity at constant pressure via the relation $c_p = c_v + R$. Thus, Equation 9 may be simplified to

$$\delta Q = c_p dT - V\,dp, \tag{10}$$

which is 0 in an adiabatic system. As V itself may be redefined in terms of p and T using the ideal gas law $pV = RT$, it is possible to rearrange the relationship to obtain a pair of differential equations relating the change in temperature of a parcel of air to a corresponding change in pressure,

$$V\,dp = c_p dT$$

$$RT\frac{dp}{p} = c_p dT$$

$$\frac{dp}{p} = \frac{c_p}{R}\frac{dT}{T}. \tag{11}$$

This equation may be integrated to give us an equation which may be solved to give a value of the potential temperature, $T_0 = \theta$ at standard pressure p_0:

$$\ln p_1 - \ln p_0 = \frac{c_p}{R}\left(\ln T_1 - \ln T_0\right)$$

$$\frac{R}{c_p}\ln\frac{p_1}{p_0} = \ln\frac{T_1}{T_0}$$

$$\left(\frac{p_1}{p_0}\right)^{\frac{R}{c_p}} = \frac{T_1}{T_0}$$

$$\theta = T\left(\frac{p_0}{p}\right)^{\frac{R}{c_p}}. \tag{12}$$

11

Table 1: Hand-calculated wind shears from the thermal wind based on Figure 7

Location	$d\theta$	Expected Shear
45°N, 500mb	$\frac{310\text{K}-292.5\text{K}}{550\text{km}} = 3.18 \times 10^{-5}\text{K/m}$	-0.206 $\frac{\text{m/s}}{\text{mb}}$
65°N, 600mb	$\frac{280\text{K}-285\text{K}}{550\text{km}} = -9.09 \times 10^{-6}\text{K/m}$	0.0516 $\frac{\text{m/s}}{\text{mb}}$
45°N, 300mb	$\frac{333\text{K}-327\text{K}}{550\text{km}} = 1.09 \times 10^{-5}\text{K/m}$	0.102 $\frac{\text{m/s}}{\text{mb}}$

It is then a simple matter to redefine the thermal wind relation in terms of the potential temperature by simply rearranging Equation 12 to give T in terms of θ and substituting the value in for T. After factoring out constant p, we obtain

$$\frac{\partial \mathbf{u}_g}{\partial p} = -\frac{R}{fp}\left(\frac{p}{p_0}\right)^{\frac{R}{c_p}} \hat{\mathbf{z}} \times \nabla \theta. \tag{13}$$

3.4 The Polar Front, the Jet Stream, and Potential Temperature

As mentioned in Section 3.2, it is possible to actually demonstrate this relationship between the (potential) temperature and the wind shear of the jet stream by calculating the wind shear by hand and comparing it with the real jet stream. In Figure 7, the cross-section previously depicted in Figure 6 is depicted with contour lines corresponding to potential temperature instead of actual temperature. Here, potential temperature *increases* with height, rather than decreasing like the air temperature.

Figure 7 also depicts the normal wind (i.e. the jet stream). It is possible to compare the numerical values of the jet stream speeds with what would be expected from Equation 13 by taking the horizontal change of theta at a single pressure level and comparing it to the rate of change of the normal wind (wind shear) across that pressure level.

The results of these calculations are given in Table 1 and may be compared with the observed shear values given in Table 2. In all cases, the expected wind shear calculated from the thermal wind proves to be relatively close to the actual values of wind shear. Note that the particular cross-section has been chosen such that the jet stream is effectively normal to the cross-section. Were it not normal, the observed "normal" wind speed would be less than the actual wind speed and would have a wind shear observed to be less than expected.

As the jet stream is a consistent phenomena, it may also be observed on climatological timescales. It is possible to show that the thermal wind relationship holds for the jet stream on even these timescales, comparing the wind shear and temperature gradients using MATLAB. Figure 8 depicts the long-term climatological average of θ at the 500mb level in January in the Northern Hemisphere.
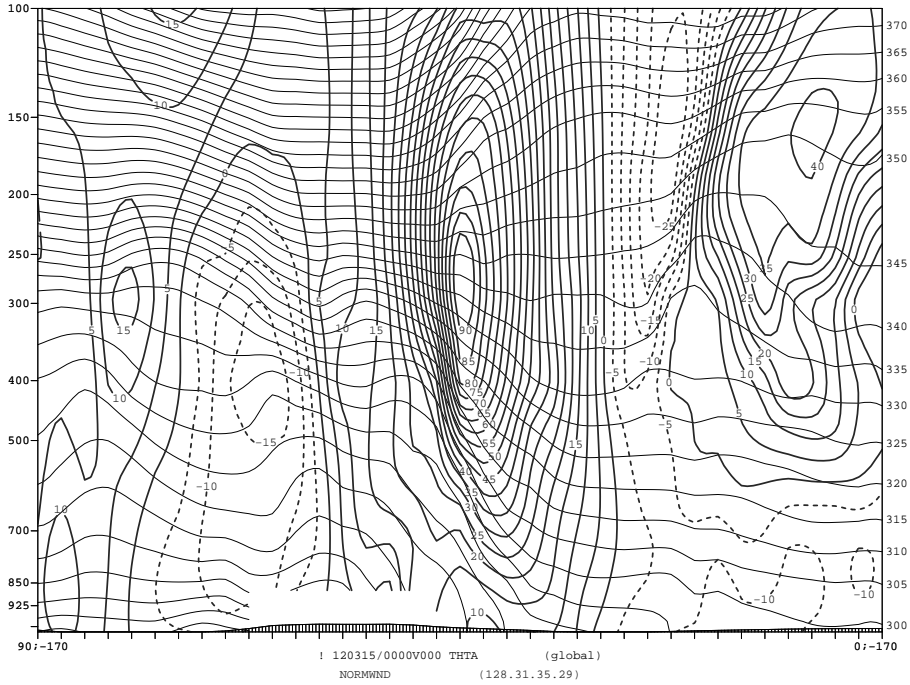
Figure 7: Cross-section of potential temperature and normal wind above 170°W longitude from the north pole to the equator as of 00:00 UTC on 15 March 2012. The strongest winds are observed above regions of strong slope in the potential temperature. In comparison with the actual air temperature in Figure 6, temperature is very stratified at higher altitudes, and potential temperature is observed to *increase* with height. Cold air is visible as a "mound" near the north pole.

Table 2: Hand-calculated wind shears from the thermal wind compared to observed values in Figure 7. The values compare reasonably well.

Location	Expected Shear	Observed Shear
45°N, 500mb	-0.206 $\frac{\text{m/s}}{\text{mb}}$	$\frac{30\text{m/s}-65\text{m/s}}{200\text{mb}} = -0.175\frac{\text{m/s}}{\text{mb}}$
65°N, 600mb	0.0516 $\frac{\text{m/s}}{\text{mb}}$	$\frac{-12\text{m/s}-(-15)\text{m/s}}{200\text{mb}} = 0.015\frac{\text{m/s}}{\text{mb}}$
45°N, 300mb	0.102 $\frac{\text{m/s}}{\text{mb}}$	$\frac{85\text{m/s}-90\text{m/s}}{200\text{mb}} = -0.025\frac{\text{m/s}}{\text{mb}}$

Figures 9 and 10 depict the longitudinal wind at the 600mb and 400mb levels over the same region and time period.

By using MATLAB to perform the same calculations performed by hand in Table 1, it is possible to obtain several plots demonstrating that the change in potential temperature from south to north at the 500mb level accurately predicts the average wind shear calculated from the 400 and 600mb winds.

In Figure 11, for example, the slope of the potential temperature along the 500mb surface between 110°E and 150°E may be observed, which is marked by a notable decrease in the potential temperature between 30°N and 60°N. The gradient of this, used in the thermal wind equation, is given in Figure 12.

The gradient can be used to calculate the expected wind shear through the use of the thermal wind relation, giving the expected wind shear profile on the left side of Figure 13. It is also possible to calculate the wind shear directly from the 600mb and 400mb winds and averaging the shear between 110°E and 150°E, given on the right side of the same figure.

It is evident that the thermal wind relation is strongly supported by the similar profiles of the two methods of calculating wind shear. Calculation of the residual of the difference between the two methods (Figure 14) reveals that the potential temperature is a remarkably accurate indicator of the wind shear, with residual errors of no more than 0.01 m/s/mb at points where the actual shear is 0.08 m/s/mb. The greatest error is observed near the equator, where the value of f used in calculating the thermal wind equation is extremely small.

3.5   Synoptic Fronts and Thermal Wind

Besides the polar front, other fronts exist in the middle latitudes, including those frontal boundaries which accompany high and low pressure systems. These synoptic fronts exhibit many of the features of the polar front, albeit on smaller scales, and it is possible to compare the results of the thermal wind equation along the polar front with these synoptic fronts.
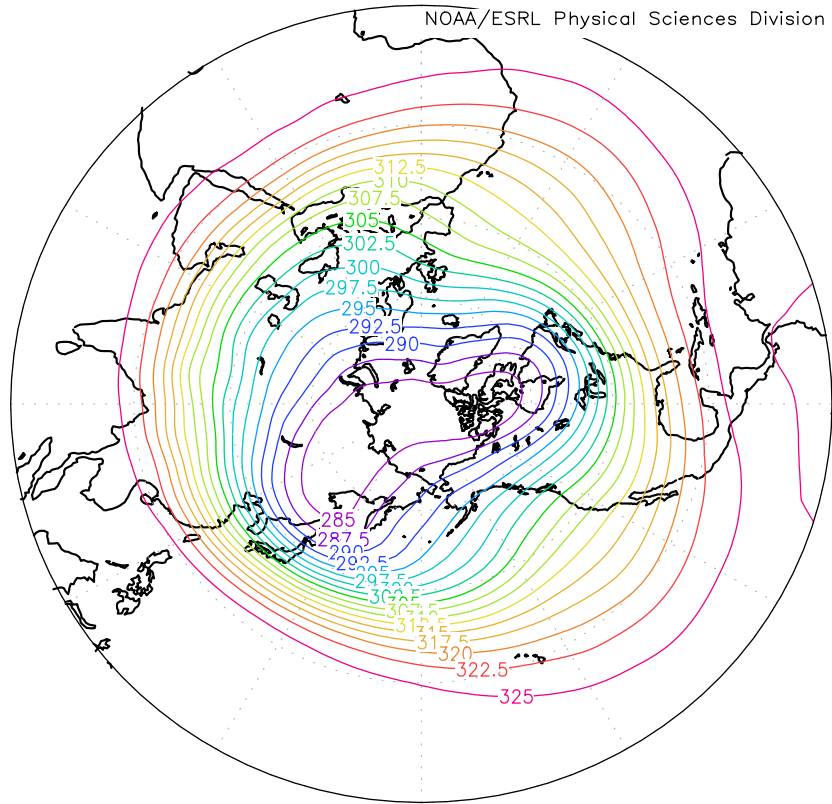
Many synoptic fronts are not zonal like the polar front; synoptic fronts generally separate distinct pressure systems, which may have broken off from the larger polar or tropical air masses due to the meandering nature of the jet stream. In such a case, synoptic fronts may have a north-south alignment rather than an east-west alignment like that of the polar front.

One such front was that responsible for the April 3, 2012, outbreak of tornadoes in the Dallas-Fort Worth region. On April 3rd, two cold fronts in close succession separated a cut-off low of cooler air (featuring surface temperatures in the 40s and 50s) from the warmer sub-tropical air near the Gulf of Mexico which featured surface temperatures in the 70s and 80s (See Figure 15).

A cross-section of the normal winds and potential temperature along the 35th

14

lon: plotted from 0.00 to 360
lat: plotted from 0 to 90.00
lev: 500.00
t: Jan

Long Term Mean pottmp degK

NOAA/ESRL Physical Sciences Division

312.5
310
307.5
305
302.5
300
297.5
295
292.5
290

285
287.5
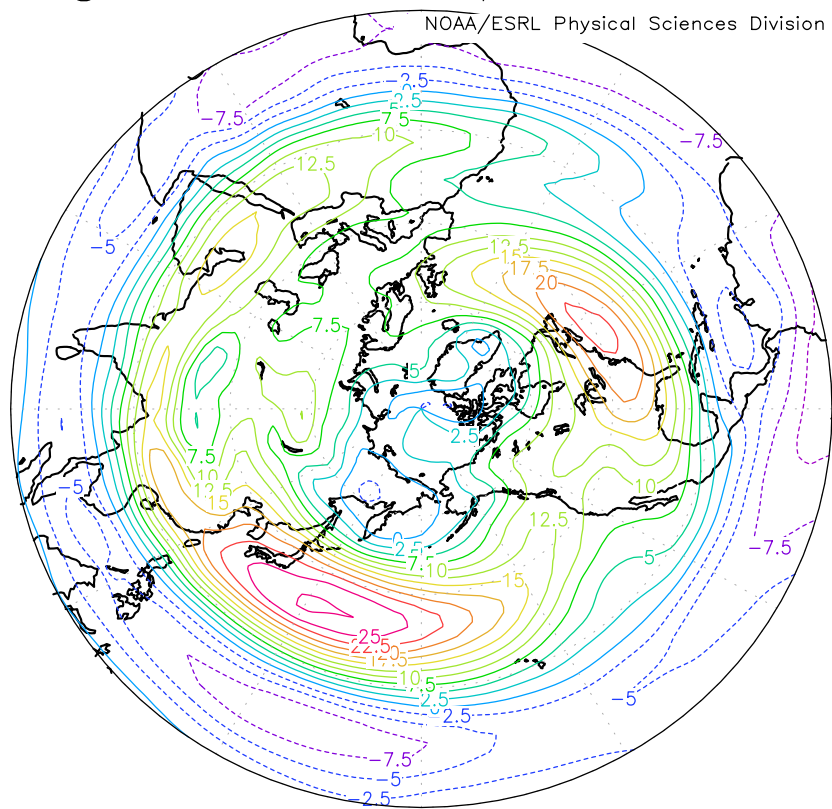290
292.5
293.5
300
305
307.5
315
317.5
320
322.5
325

NCEP Reanalysis Products Pressure Level GrADS image

MAX=328.012
MIN=282.527

Figure 8: Monthly long-term mean potential temperature at the 500mb level in January in the Northern Hemisphere. The climatological data covers the years 1968 through 1996. Here, sharp potential temperature gradients are observable, especially over the oceans.

lon: plotted from 0.00 to 360
lat: plotted from 0 to 90.00
lev: 600.00
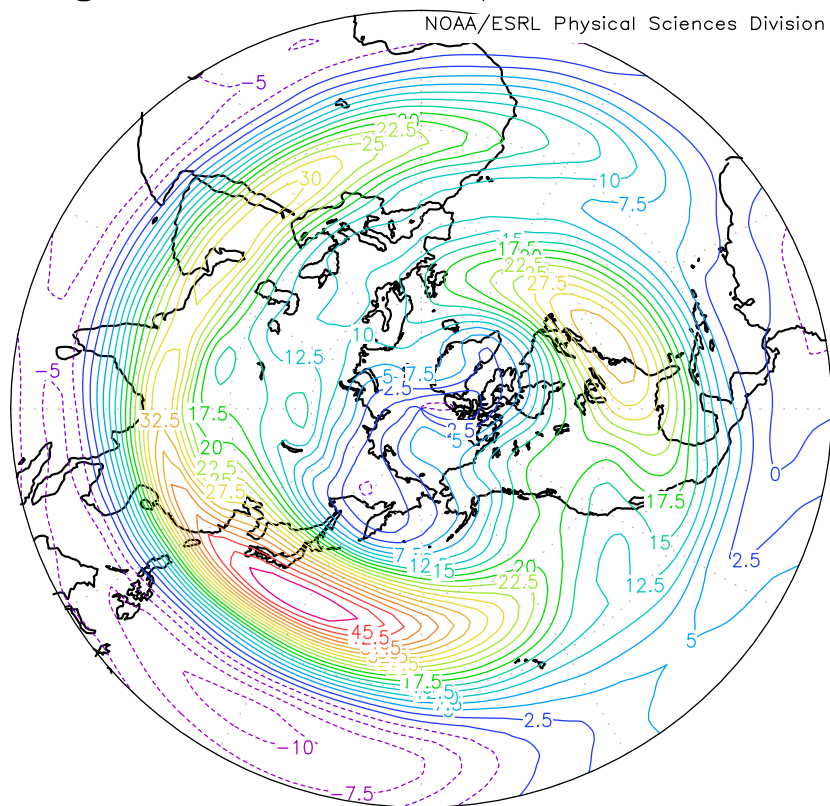t: Jan

Long Term Mean uwnd m/s

NCEP Reanalysis Products Pressure Level GrADS image

Figure 9: Monthly long-term mean zonal wind speed at the 600mb level in January in the Northern Hemisphere. The climatological data covers the years 1968 through 1996. Winds are greatest near the regions of greatest potential temperature gradient.

lon: plotted from 0.00 to 360
lat: plotted from 0 to 90.00
lev: 400.00
t: Jan

Long Term Mean uwnd m/s

NOAA/ESRL Physical Sciences Division

NCEP Reanalysis Products Pressure Level GrADS image

Figure 10: Monthly long-term mean zonal wind speed at the 400mb level in January in the Northern Hemisphere. The climatological data covers the years 1968 through 1996. Winds are greatest near the regions of greatest potential temperature gradient.

500mb surface for January, 110deg E to 150deg E

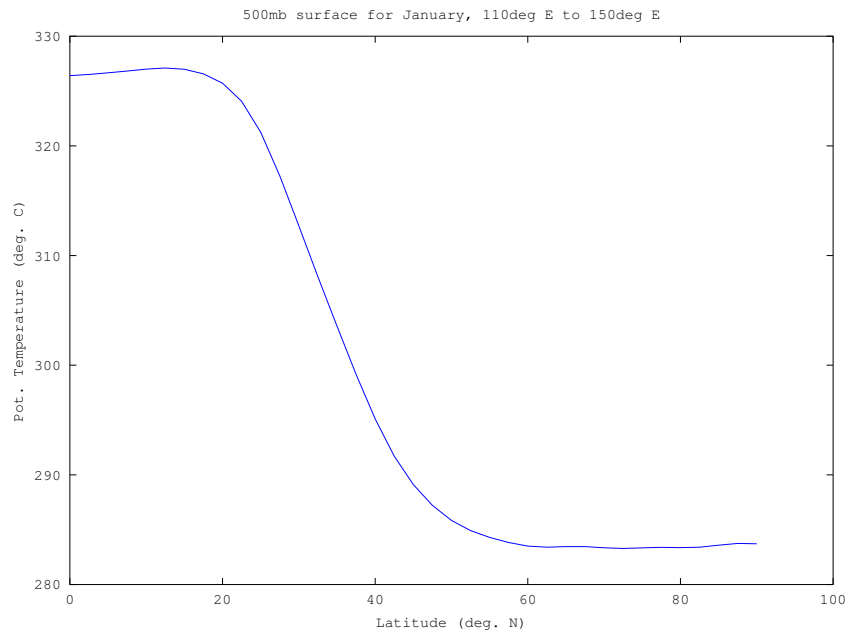Pot. Temperature (deg. C)

Latitude (deg. N)

Figure 11: Cross-section of the long-term mean potential temperature at the 500mb level in January in the Northern Hemisphere, averaged between 110°E and 150°E. The climatological data covers the years 1968 through 1996. Potential temperature decreases significantly between 30°N and 60°N, representing the polar front.
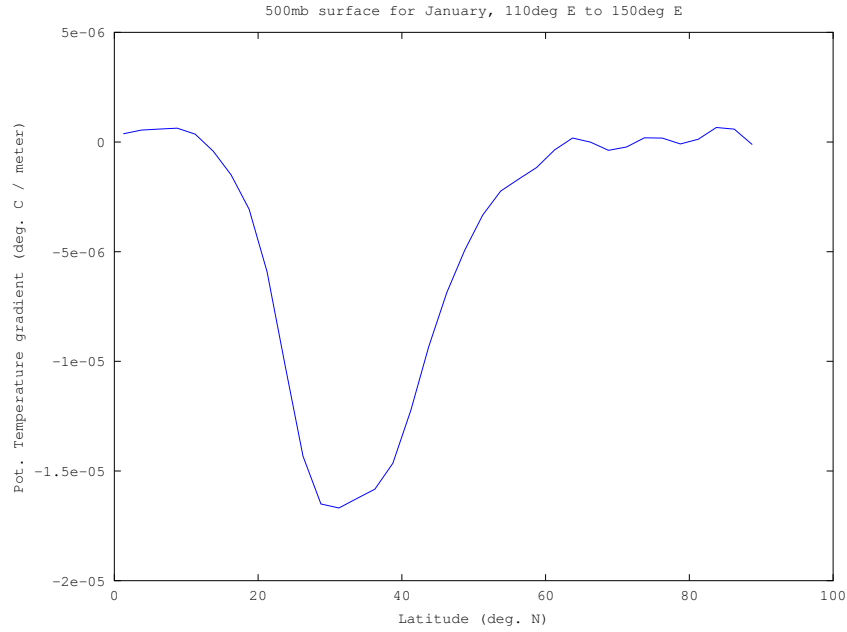
Figure 12: Cross-section of the gradient of the long-term mean potential temperature at the 500mb level in January in the Northern Hemisphere, averaged between 110°E and 150°E. The climatological data covers the years 1968 through 1996. Potential temperature decreases significantly between 30°N and 60°N, representing the polar front.
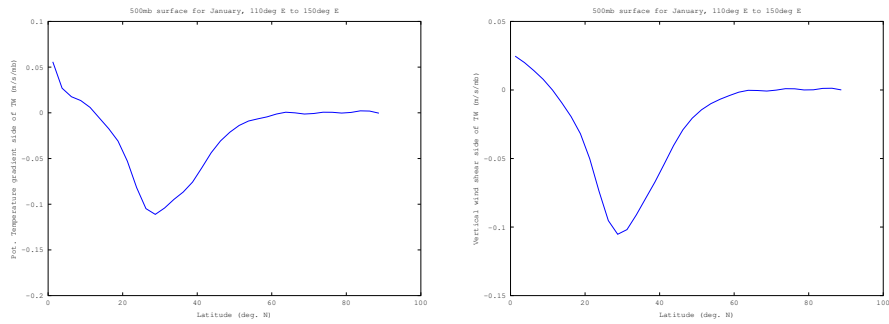

Figure 13: Cross-section of the expected wind shear calculated using the potential temperature gradient (*left*) and the observed wind shear as calculated from the 600mb and 400mb wind speeds (*right*) at the 500mb level in January in the Northern Hemisphere, averaged between 110°E and 150°E. The climatological data covers the years 1968 through 1996. Shear is strongest between 30°N and 60°N, along the polar front.

19

500mb surface for January, 110deg E to 150deg E

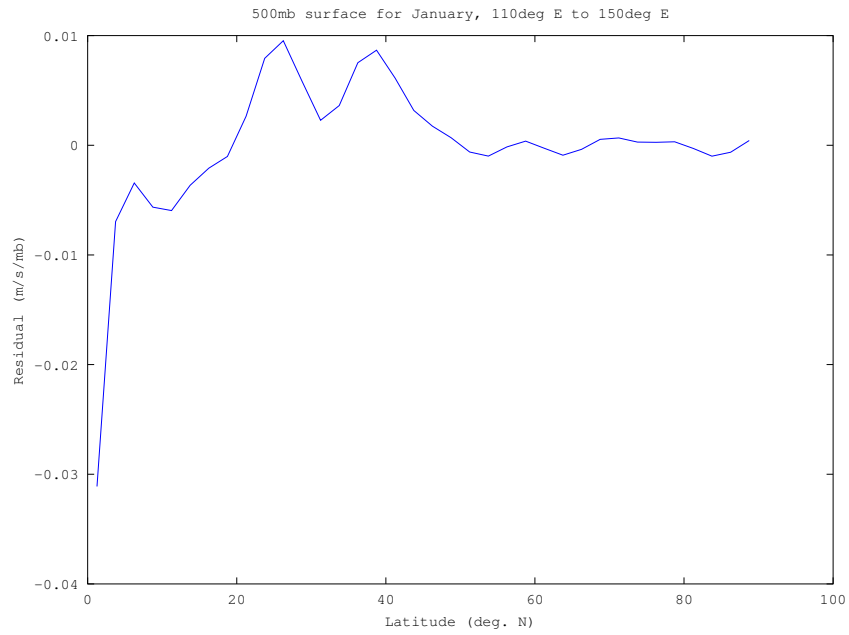Residual (m/s/mb)

Latitude (deg. N)

Figure 14: Cross-section of the residual difference between the wind shear as calculated using the potential temperature, and that calculated directly from the wind speeds of the 600mb and 400mb levels, based upon of the long-term mean potential temperature at the 500mb level in January in the Northern Hemisphere, averaged between 110°E and 150°E. The climatological data covers the years 1968 through 1996. The residual error is at most only 0.1 m/s/mb, and is generally less than 1/8th of the actual value.
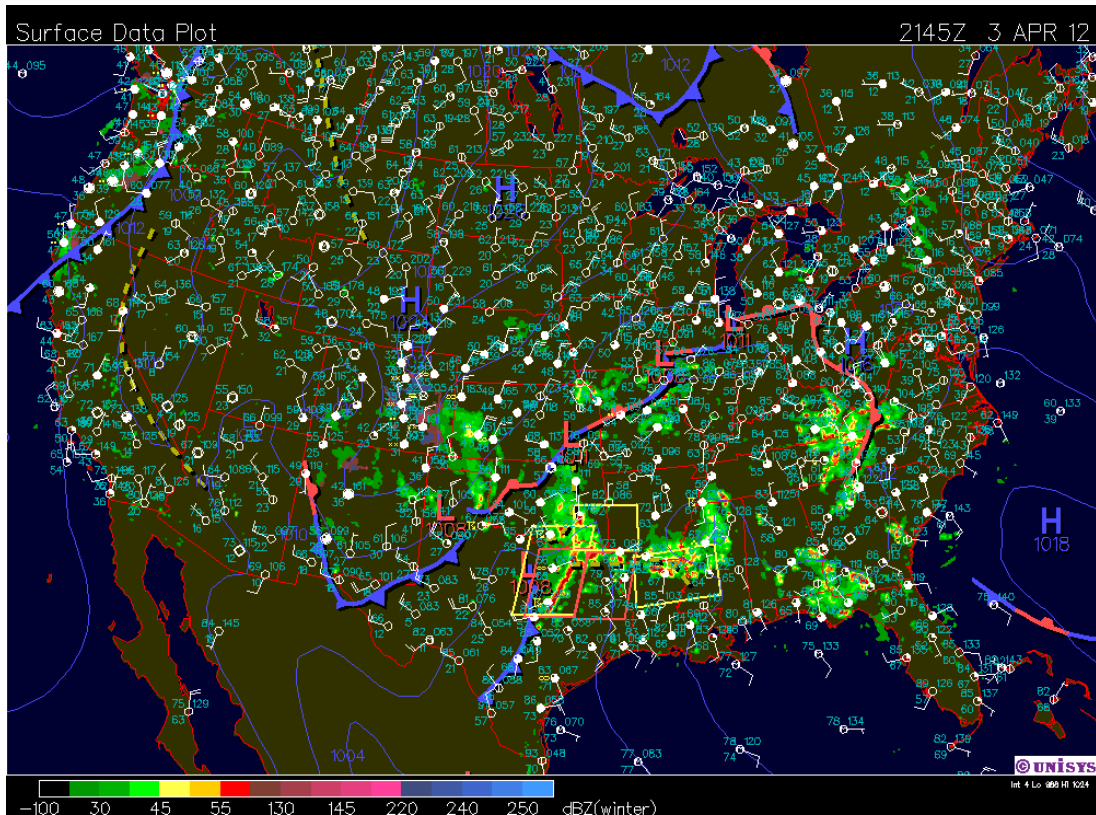
20

Figure 15: Surface conditions and surface frontal boundaries as of 21:45 UTC on April 3, 2012 shortly after the outbreak of tornadoes in the Dallas-Fort Worth area ended. [1] The frontal boundary responsible sits slightly behind the radar-observable precipitation.

parallel across which the frontal boundary moved (Figure 16) reveals not only the mass of cold air behind the frontal boundary at around 100°W, but also exhibits relatively strong vertical shear above the boundary as might be expected.

What is interesting about this observation is its relevance to the outbreak of tornadoes itself. Although the squall line itself moved from west to east, it may be observed that the individual supercells (and the tornadoes that accompanied them) moved from south-south-west to north-north-east (Figure 17), more closely following the path of the upper-level thermal wind than the movement of the front!

3.6 The Slope of Potential Temperature and the Margules Formula

Careful observation of Figure 7 reveals a sharply defined slope in the potential temperature contours below the jet stream. This makes intuitive sense; after all, a horizontal potential temperature gradient must have a vertical component as well as air is continuous. It is just this continuity, however, which permits the derivation of this slope from the temperature gradient itself using a relation known as the Margules Formula. [5]

The Margules Formula may be derived from the thermal wind equation by considering the difference in wind speeds above and below a discrete boundary layer separating two temperature regimes. If Equation 13 is evaluated at two distinct points within a north-south cross-section (i.e. examining the x-component, as the normal wind is considered), the following relationship is obtained:

$$\frac{u_1 - u_2}{p_1 - p_2} = \frac{R}{fp} \left(\frac{p}{p_0} \right)^{\frac{R}{c_p}} \frac{\theta_1 - \theta_2}{y_1 - y_2}. \tag{14}$$

We may rearrange this relationship to obtain an equation for the discrete change in velocity in terms of the slope $\frac{\Delta p}{\Delta y} = \tan \gamma$, where γ is the angle of the slope:

$$u_1 - u_2 = \frac{R}{fp} \left(\frac{p}{p_0} \right)^{\frac{R}{c_p}} (\theta_1 - \theta_2) \frac{\Delta p}{\Delta y}$$

$$= \frac{R}{fp} \left(\frac{p}{p_0} \right)^{\frac{R}{c_p}} (\theta_1 - \theta_2) \tan \gamma. \tag{15}$$

It is thus possible to derive the expected angle of the interface between two potential temperature surfaces from the wind shear and temperature gradient at a given point.
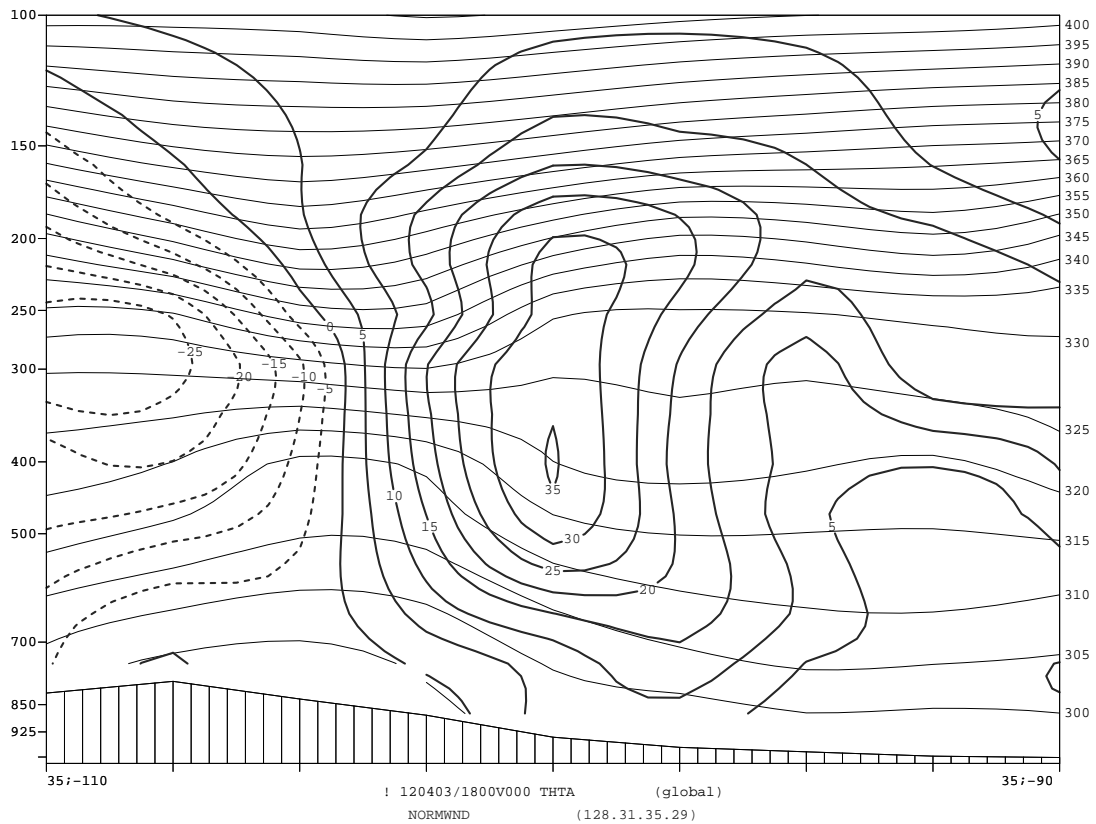
Figure 16: Cross-section of potential temperature and normal wind above 35°N latitude from 110°W to 90°W as of 18:00 UTC on 3 April 2012. A decrease in potential temperature may be observed corresponding with the cold front near 100°W. Thermal wind shear may also be observed to be greatest at the frontal boundary.
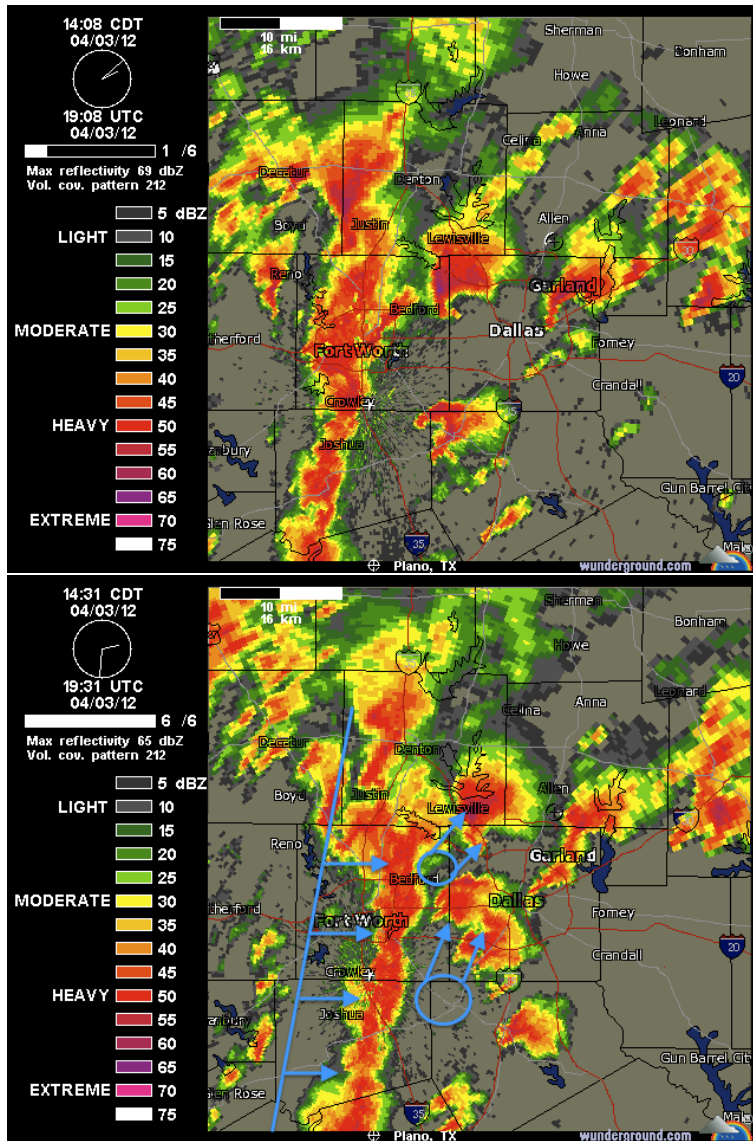
Figure 17: Radar observations of the Dallas-Fort Worth tornado outbreak taken 20 minutes apart at 19:08 and 19:31 UTC, April 3, 2012. [2] Supercells along the squall line responsible for the Dallas-Fort Worth tornado outbreak were observed to move from south-south-west to north-north-east, following the thermal wind rather than the movement of the boundary itself.

Table 3: Hand-calculated slopes of θ contours calculated using the Margules Formula, calculated from values in Figure 7.

Location	Observed 5° Δu	Observed 5° $\Delta\theta$	Expected Slope ($\frac{\Delta p}{\Delta y}$)
45°N, 500mb	$55 - 25 = 30$m/s	17.5K	$2.65 \times 10^{-4}\frac{\text{mb}}{\text{m}}$
65°N, 600mb	$-10 - (-12.5) = 2.5$m/s	-5K	$-2842\frac{\text{mb}}{\text{m}}$
45°N, 300mb	$90 - 55 = 35$m/s	6K	$6.25 \times 10^{-4}\frac{\text{mb}}{\text{m}}$

Table 4: Hand-calculated slopes of θ contours compared to observed values in Figure 7. The values compare reasonably well near the jet stream, but are less accurate at more stable locations.

Location	Expected Slope ($\frac{\Delta p}{\Delta y}$)	Observed Slope
45°N, 500mb	$2.65 \times 10^{-4}\frac{\text{mb}}{\text{m}}$	$\frac{350-275\text{mb}}{550\text{km}} = 1.36 \times 10^{-4}\frac{\text{mb}}{\text{m}}$
65°N, 600mb	$-2842\frac{\text{mb}}{\text{m}}$	$\frac{530-625\text{mb}}{550\text{km}} = -1.72 \times 10^{-4}\frac{\text{mb}}{\text{m}}$
45°N, 300mb	$6.25 \times 10^{-4}\frac{\text{mb}}{\text{m}}$	$\frac{630-400\text{mb}}{550\text{km}} = 4.18 \times 10^{-4}\frac{\text{mb}}{\text{m}}$

It is possible to check the validity of the Margules Formula for each of the three locations in Tables 1 and 2 by calculating the expected slope at each point from the observed shear and observed $d\theta$ and compare this with the slopes of the θ contour lines near each point. These values are calculated and given in Table 3 and compared to the observed values in Table 4, which shows that Margules' formula holds reasonable well near the jet stream.

Points further from the jet stream seem less reliable, but this could be due to the higher latitude and (more importantly) much lesser wind shears involved. The smaller changes in u and θ at the 65°N point mean that additional accuracy is needed in order to obtain an accurate slope. Furthermore, the Margules Formula assumes that geostrophic flow predominates. Although the correspondence of the thermal wind equation would seem to indicate that it does, it is possible that the Margules Formula is more sensitive to changes in the Rossby number than the thermal wind equation.

4 An Experiment: Thermal Wind Along Salinity Boundaries

The thermal wind phenomenon may also be tested experimentally through the use of a rotating tank containing salt water and fresh water. The salt water, being denser than the fresh water, serves as a proxy for cold air in the rotating frame and may form a cone shape. This cone can then be used to test the Margules Formula, and by extension, the concept of thermal wind.

In such an experiment, it is important to consider the difference between com-

pressible fluids like the atmosphere and incompressible fluids such as the water in this experiment. Thus, it is critical that the thermal wind equation be presented and worked with in *height* coordinates rather than *pressure* coordinates. Furthermore, density is measured *directly* rather than working with temperature as a proxy.

Thus, instead of taking the derivative of the geostrophic wind in constant pressure coordinates, Equation 3, with respect to pressure, we will take the derivative of the geostrophic wind in constant *height* coordinates,

$$\mathbf{u}_g = \frac{1}{\rho f} \hat{\mathbf{z}} \times \nabla p, \tag{16}$$

and substitute the hydrostatic equation, Equation 4, directly, giving:

$$\frac{\partial \mathbf{u}_g}{\partial z} = -\frac{g}{\rho_0 f} \hat{\mathbf{z}} \times \nabla \rho. \tag{17}$$

Note that an additional ρ value has been introduced, such that the original ρ has been substituted by a value ρ_0 representing a constant *reference density* from which the density of any one fluid parcel, ρ varies by only a small amount, $\rho = \rho_0 + d\rho, \frac{d\rho}{\rho_0} \ll 1$.

It is possible to re-derive the Margules Formula from this alternate representation as well, simply by following the steps we made to work with the thermal wind equation discretely in Section 3.6. Thus, we consider a quantifiable discrete boundary of density within the fluid by examining two points, n_1 and n_2, where the density is ρ_1 at n_1 and ρ_2 at n_2:

$$\frac{u_1 - u_2}{z_1 - z_2} = -\frac{g}{\rho_0 f} \frac{\rho_1 - \rho_2}{x_1 - x_2}. \tag{18}$$

We may rearrange this relationship to obtain an equation for the discrete change in velocity in terms of the slope $\frac{\Delta z}{\Delta x} = \tan \gamma$, where γ is the angle of the slope:

$$u_1 - u_2 = -\frac{g}{\rho_0 f} \left(\rho_1 - \rho_2 \right) \frac{\Delta z}{\Delta x}$$

$$= -\frac{g}{\rho_0 f} \left(\rho_1 - \rho_2 \right) \tan \gamma. \tag{19}$$

4.1 The Experimental Setup

Given that it is possible to achieve meaningful density differences using water of different salinity, it would be possible to determine the validity of the Margules
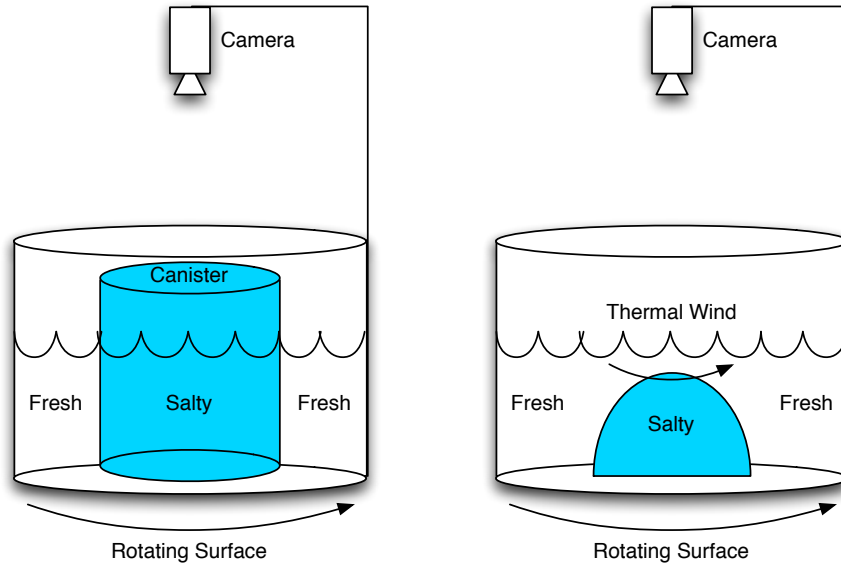
Figure 18: The experimental setup. On the left, salty water is placed in a canister separated from the remainder of the tank through the use of Vaseline to seal the bottom of the canister. On the right, the canister is removed, leaving the salty water to reach equilibrium by forming a cone in the rotating frame.

Formula and thermal wind by constructing an experiment featuring a rotating tank in which water of two different salinities (and thus two different densities) would be placed. In principle, the water of greater density would form a cone near the center of the rotation, much like the potential temperature cone observed over the north pole in Figure 7.

In order to prevent thorough mixing of the water, this may be achieved by placing a canister with no bottom in the center of a rotating tank, taking care to seal the bottom of the canister against water intrusion through the use of Vaseline. The outer region of the rotating tank may then be filled with less dense fresh water, while colored salt water may be prepared and placed in the center canister once solid-body rotation is observed with the fresh water (left side of Figure 18).

The achievement of solid-body rotation may be determined through use of a camera which co-rotates with the rotating tank. When solid-body rotation is achieved, water in the tank (specifically, a paper dot placed on the water in the tank), as viewed from the camera, would appear to no longer be rotating.

Once this is accomplished, water within the canister is evacuated to a reasonable extent and is replaced with water having a higher salinity (and thus a higher

Table 5: Measurements of water density in the rotating tank experiment.

Measurement	Mass	Volume	Density
Fresh Water	100.6 ± 0.05g	100 ± 0.25mL	$1006 \pm 3 \frac{\text{kg}}{\text{m}^3}$
Salt Water	116.8 ± 0.05g	99.7 ± 0.25mL	$1171.5 \pm 3.5 \frac{\text{kg}}{\text{m}^3}$
Salt Water (in canister)	62.4 ± 0.05g	55.8 ± 0.25mL	$1118 \pm 6 \frac{\text{kg}}{\text{m}^3}$

density). Finally, the canister may be removed by simply pulling it upwards. As the canister lacks a bottom, the denser salty water will now find equilibrium with the lighter fresh water rising above it, creating a cone shaped structure (right side of Figure 18).

This cone should exhibit thermal wind appropriate to the density difference of the salt water and fresh water. This could be measured by tracking particles placed on the top of the water using particle-tracking software and the co-rotating camera, as the thermal wind is observed relative to the rotating frame. The particle speeds observed should be related to the slope of the cone via the density-based version of the Margules Formula and the density of the fluid inside the cone and that outside the cone.

4.2   Experimental Observations

My partner, Allison Schneider, and I performed this experiment once in a rotating tank rotating at 2545 ± 10 milli-eff (i.e. $f = 2\omega = 2.545 \pm 10 \frac{\text{rad}}{\text{s}}$). We additionally measured the mass a volume of both the fresh and salty water used in the tank prior to the beginning of the experiment. In addition, as we were unable to completely evacuate the innermost cylinder, we took an additional measurement of the inner-cylinder's mass before removing the canister. The mass was measured by way of an electronic scale which had been zeroed based on the dry mass of a graduated cylinder for measuring volume. These measurements are given in Table 5.

Upon raising the canister and releasing the salty water, a cone was indeed observed, and a dip in the surface of the water appeared over the center of the cone. This dip corresponds to the lower overall height of a cylinder of the denser fluid which has, at its bottom, a pressure equal to that of the less dense fluid on the outside of the cone. A rough observation of the depth of the dimple was about 1cm in a tank that was about 20cm deep. Thus, the height of the water at the center of the cone was about 5% lower than the height of the water elsewhere in the tank. Given the hydrostatic relation $p = \rho g h$, this corresponds well with the observed density of the salt water being between 10-20% greater than the density of the surrounding fresh water.

Dots were placed on the surface of the water above the cone, and a thermal wind-like movement was observed to move counter-clockwise around the center of the cone in the rotating frame, as depicted by the tracks in Figure 19. From
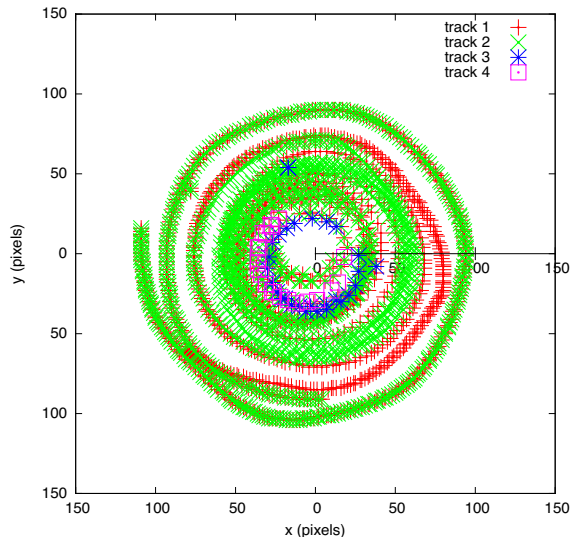
Figure 19: The set of tracks formed by particles which moved around the cone of denser, salty water in the rotating frame. These tracks have been normalized from video in which coordinates were measured from the top-left corner of the frame, and are depicted in polar coordinates. Radius is measured in pixel units relative to the size of the camera's viewing angle. There are approximately 10 pixels to the cm in the recorded video. Several points were cleaned and removed from the tracks as noise.

these measurements, it was possible to derive angular velocities for the dots by first calculating an approximate angular velocity by averaging the angular velocity between a point and its previous point, and the angular velocity between a point and its following point. These values could then be multiplied by an an estimate of the radius in order to obtain angular velocities. As the exact radii were not known with certainty (due to an estimate of the ratio of pixels to centimeters), error was introduced into the observed estimated velocities, given in Figure 20.

4.3   Analysis of the Tracks

If the velocity of the liquid is assumed to be 0 at the bottom of the tank, it is then possible to use the provided densities to estimate the angle of the cone according to the density formulation of Margules Formula, Equation 19. This includes additional error introduced by the error in the measurement of the two densities, resulting in a plot with significant error bars (Figure 21). However, about two-thirds of this error stems from the initial error in the ratio of pixels to centimeters. Error bars are much improved if no error is assumed in this
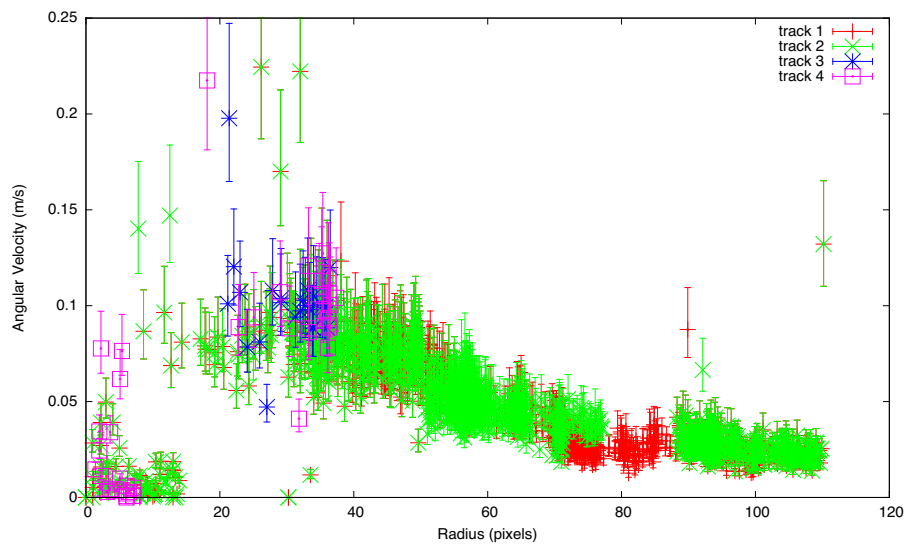
29

Figure 20: The observed velocities of particles which moved around the cone of denser, salty water, plotted relative to their radius. Velocities are relative to the rotating frame. Radius is measured in pixel units relative to the size of the camera's viewing angle. There are approximately 10 ± 2 pixels to the cm in the recorded video, the error of which translates into error in the estimated velocities. Points with negative or extremely high velocities have been cropped from the output as noise.
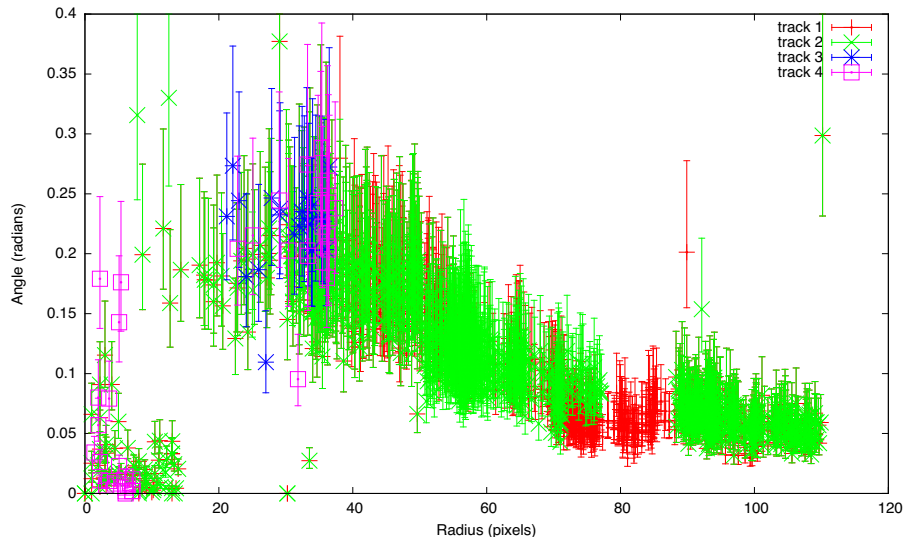
Figure 21: Estimated angle of the side of the cone of denser salty water derived from the velocities in Figure 20 and using the densities given in Table 5. Although the error bars are significant, it is still possible to see that the angle is greatest at the points of greatest velocity, where angle decreases towards the outside of the cone.

measurement (Figure 22).

We may compare these predicted angles with the actual angle of the cone, based on several pictures we took of the cone during our experiment. Unfortunately, due to a lack of clear metrics and few clear images, measuring the angle of the cone is the most error-prone part of this experiment, as can be seen in the two figures, Figure 23 and Figure 24.

In both images, the angle is observed to be nearly four times the greatest angle estimated from the particle velocities. Even when errors in radial estimation are included, the angle is still off by a factor of two. This discrepancy suggests that there exists some unaccounted for error in these results. Although the angle of the photograph in Figure 23 might suggest that the error might arise from refraction from the water-air transition, the fact that Figure 24, which is taken almost edge-on, has nearly the same profile suggests that this is not a reasonable argument.

A more plausible contributing factor is based on our assumption that the bottom of the liquid is stationary. Although not quantified in our experiment, this assumption is not completely true. There is actually a slight counter-clockwise flow near the bottom of the tank, due in part to the mixing and settling of the salty water due to gravity. As this movement is opposite that observed on
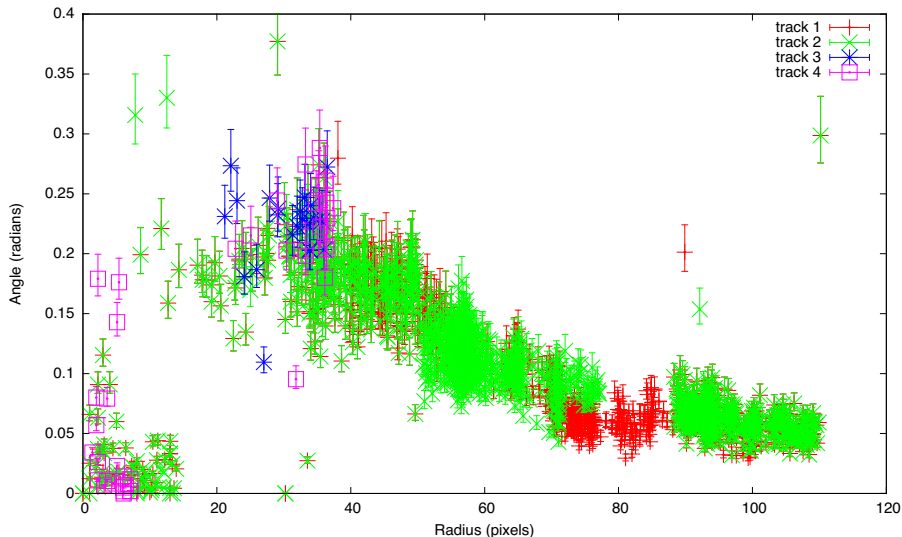
31

Figure 22: Estimated angle of the side of the cone of denser salty water derived from the velocities in Figure 20 and using the densities given in Table 5, and assuming no error in the estimated velocities.

the surface (which is counter-clockwise), the amount of shear is actually greater than the observed surface movement would otherwise imply. However, cursory visual estimates of the bottom-flow suggest that it comparatively slow, on the order of millimeters per second. Thus, the bottom flow is relatively insignificant compared to the velocities on the order of 10 cm/s observed at the surface. Thus, another explanation is warranted.

A more plausible argument for this discrepancy may lie in another assumption we have made about thermal wind. In constructing the the thermal wind equation, we assumed that geostrophic motion held. Thus, the thermal wind equation itself should only hold for movement in which the Rossby number $Ro \ll 1$. If the movement of the particles was observed to obey gradient wind or cyclostrophic flow (i.e. $Ro \gtrless 1$), the assumptions underpinning the application of the thermal wind equation would no longer hold, as the observed speed would be less than the geostrophic speed due to the influence of cyclostrophic motion. A simple analysis of the Rossby number at each radius (Figure 25), calculated as $Ro = \frac{\omega}{f}$ reveals that this is the case near the point of greatest slope and greatest velocity, potentially explaining the discrepancy in our observed velocities.
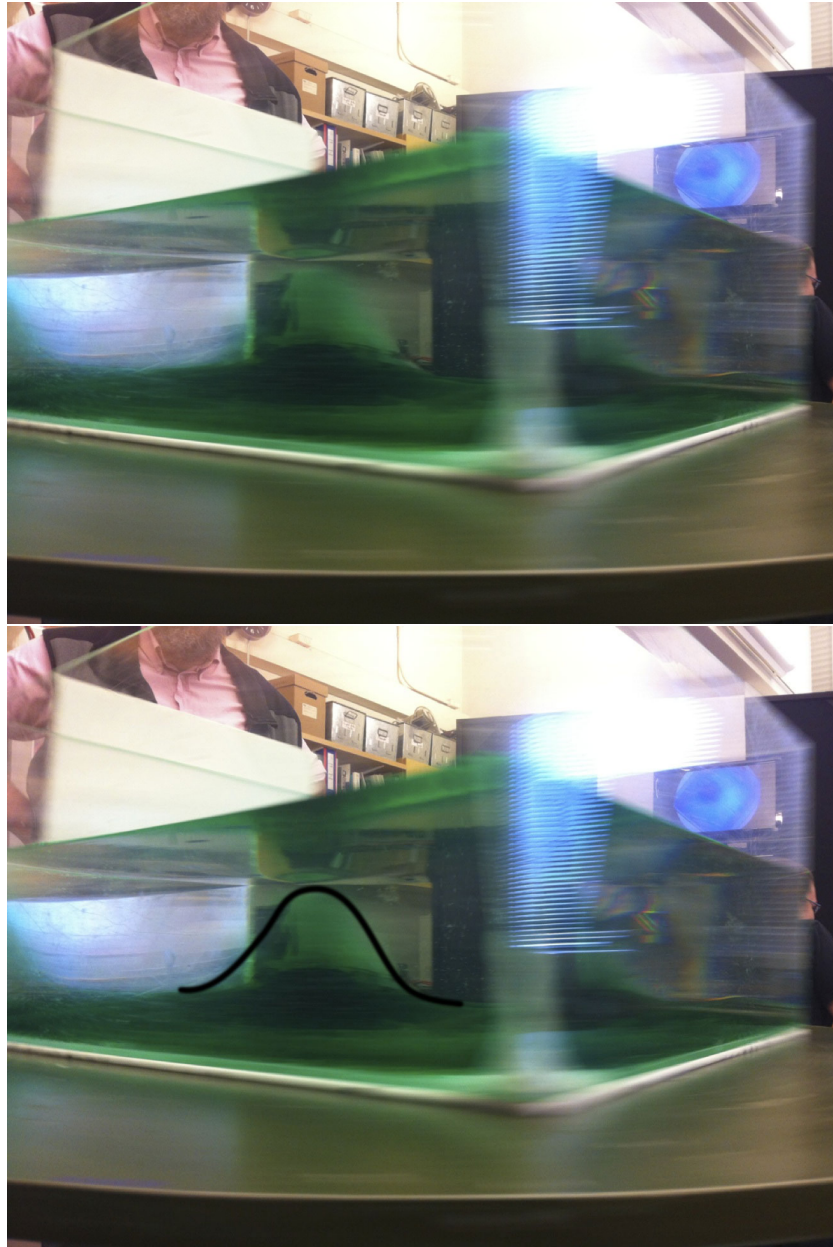
Figure 23: A photo of the cone observed in the experiment and, although not entirely clear, the estimated boundary of the cone. The angle of the cone at its steepest point is about 60°, or about 1.05 radians.
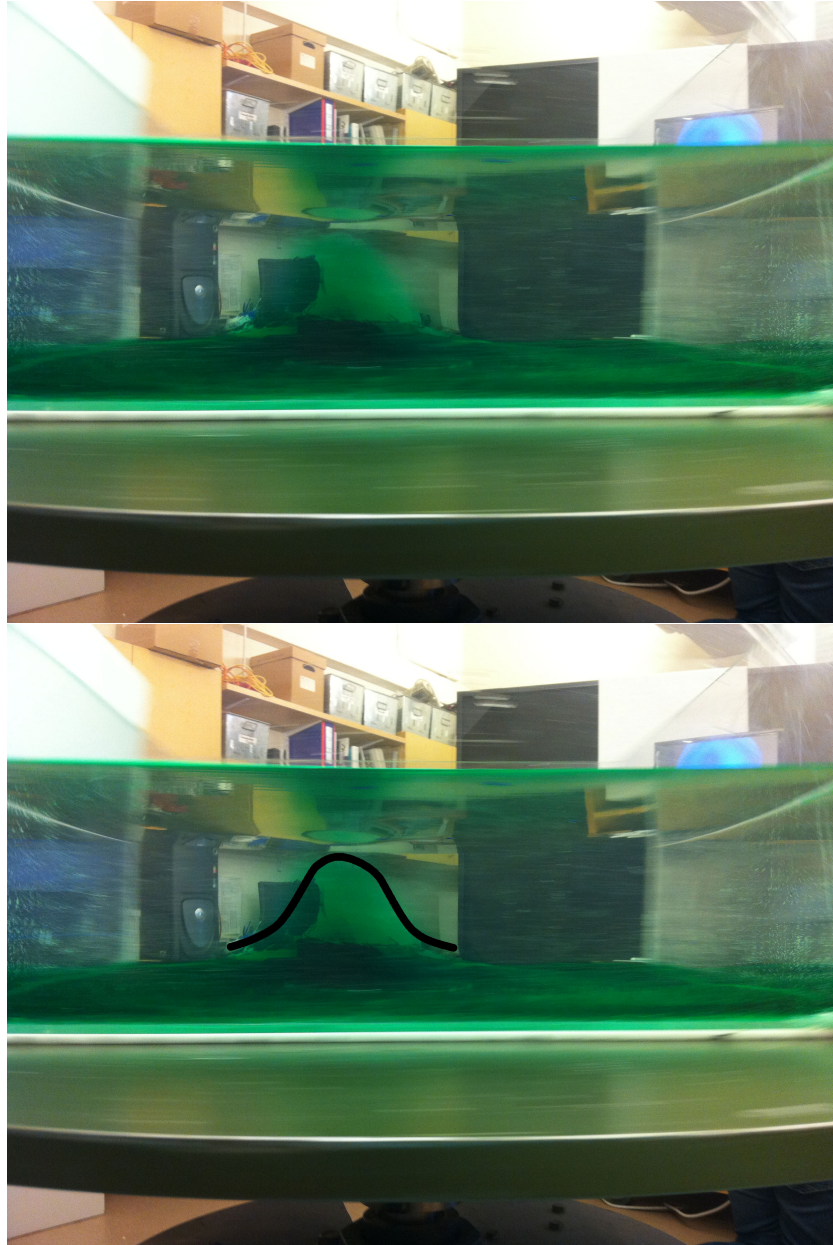
Figure 24: A photo of the cone observed in the experiment as observed from another angle and, although not entirely clear, the estimated boundary of the cone. The angle of the cone at its steepest point is about 60°, or about 1.05 radians.
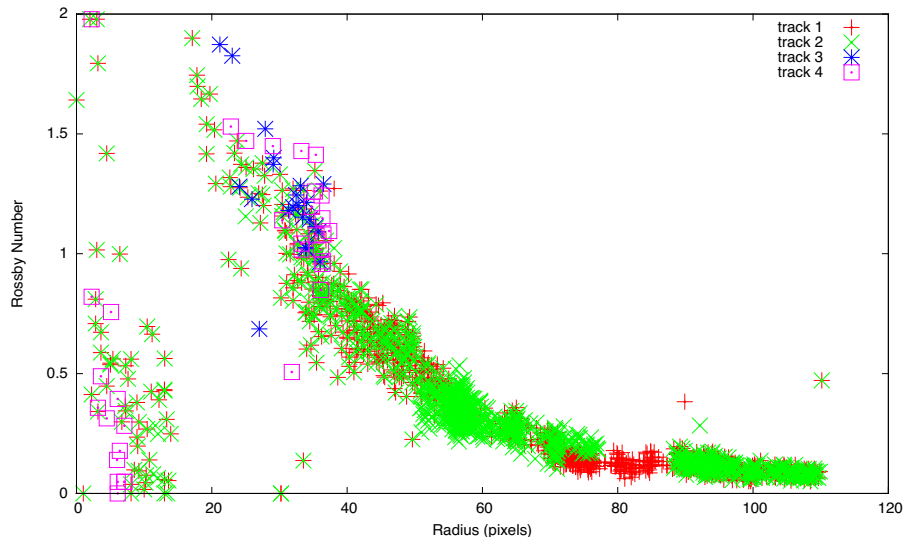
Figure 25: Rossby numbers of points as derived from angular velocity at each point and the rotational rate of the tank ($f = 2\omega = 2.545$). Rossby number is on the order of one near the point of greatest slope, suggesting that the thermal wind equation does not hold at that point.

5   Conclusions

Despite the failure of the thermal wind equation to hold at the point of greatest slope in the lab experiment, the creation of a visible vortex and a surface flow in the rotating frame supports the theory of thermal wind in a qualitative sense. In a quantitative sense, however, the thermal wind equation appears to be more readily demonstrated through global meteorological and climatological data, where geostrophic flow is more easily assumed. Indeed, some of the most compelling evidence in support of the thermal wind lies in the existence of the jet stream and its behavior which is closely predicted by the thermal wind equation.

As the jet stream plays a significant role in global weather patterns in the middle-latitudes, an understanding of the thermal wind proves critical to an improved understanding of the mechanics underpinning global-scale meteorology. However, the relevance of thermal wind suggests that understanding of a more fundamental component is needed to fully grasp the mechanics of meteorological phenomena: that of temperature.

Temperature clearly plays a role in the creation of weather phenomena, if only for its relation to the jet stream and its relationship to the movement of individual storms in a squall line. Even so, knowledge of the thermal wind does not reveal *how* the temperature gradients form in the atmosphere. How does

temperature evolve over time? Does temperature have any other effects in day-to-day meterological phenomena? Only with answers to these questions can we gain a better understanding of how the jet stream and thermal wind directly impact our lives.

References

[1] 21:45 UTC, April 3, 2012 surface data plot. Published by Unisys Weather. http://weather.unisys.com/surface/sfc_map.php?inv=0&t=cur&region=us &expanddiv=hide_bar . Archived surface maps are also available in 12 hour intervals (i.e. 12:15 UTC and 00:15 UTC) at http://weather.unisys.com/archive/sfc_map/1204/. Retrieved April 3, 2012.

[2] Animation: Six processed radar images of Dallas-Fort Worth area between 19:08 and 19:31 utc, April 3, 2012. Originally published by wunderground.com. Image later retrieved from http://i.imgur.com/3Dg0U.gif. Retrieved April 3, 2012.

[3] John A. Dutton. *Dynamics of Atmospheric Motion.* Dover Publications, 1986.

[4] James R. Holton. *An Introduction to Dynamic Meteorology.* Academic Press, third edition, 1992.

[5] Elmar R. Reiter. *Jet-Stream Meteorology.* The University of Chicago Press, 1963.